A&A 606, A90 (2017)
DOI: 10.1051/0004-6361/201731544

Astronomy & Astrophysics

Gaia and VLT astrometry of faint stars: Precision of *Gaia* DR1 positions and updated VLT parallaxes of ultracool dwarfs⋆

P. F. Lazorenko[1] and J. Sahlmann[2]

[1] Main Astronomical Observatory, National Academy of Sciences of the Ukraine, Zabolotnogo 27, 03680 Kyiv, Ukraine
e-mail: laz@mao.kiev.ua
[2] Space Telescope Science Institute, 3700 San Martin Drive, Baltimore, MD 21218, USA

Received 10 July 2017 / Accepted 1 August 2017

ABSTRACT

Aims. We compared positions of the *Gaia* first data release (DR1) secondary data set at its faint limit with CCD positions of stars in 20 fields observed with the Very Large Telescope (VLT) FORS2. We aim at an independent verification of the DR1 astrometric precision taking advantage of the FORS2 position uncertainties which are smaller than one milli-arcsecond (mas).
Methods. In the fields that we observed with FORS2, we projected the *Gaia* DR1 positions into the CCD plane, performed a polynomial fit between the two sets of matching stars, and carried out statistical analyses of the residuals in positions.
Results. The residual root mean square (rms) roughly matches the expectations given by the *Gaia* DR1 uncertainties, where we identified three regimes in terms of *Gaia* DR1 precision: for $G \simeq 17-20$ stars we found that the formal DR1 position uncertainties of stars with DR1 precisions in the range of 0.5–5 mas are underestimated by 63 ± 5%, whereas the DR1 uncertainties of stars in the range 7−10 mas are overestimated by a factor of two. For the best-measured and generally brighter $G \simeq 16-18$ stars with DR1 positional uncertainties of <0.5 mas, we detected 0.44 ± 0.13 mas excess noise in the residual rms, whose origin could be in both FORS2 and *Gaia* DR1. By adopting *Gaia* DR1 as the absolute reference frame, we refined the pixel scale determination of FORS2, leading to minor updates to the parallaxes of 20 ultracool dwarfs that we published previously. We also updated the FORS2 absolute parallax of the Luhman 16 binary brown dwarf system to 501.42 ± 0.11 mas.

Key words. astrometry – methods: data analysis – surveys – catalogs – parallaxes – stars: individual: WISE J104915.57–531906.1

1. Introduction

Gaia's first data release (DR1) provides accurate astrometric and photometric data for about one billion stars in the magnitude range $G \simeq 3-20.7$ (Gaia Collaboration 2016a,b). Independently of the mission's own validation effort (Arenou et al. 2017), several studies have found generally excellent agreement between external measurements and parallaxes (e.g. Gaia Collaboration 2017; Casertano et al. 2017) and proper motions (e.g. van der Marel & Sahlmann 2016; Watkins & van der Marel 2017) of bright stars in the *Gaia* DR1 primary data set (Lindegren et al. 2016). The bulk content of DR1, however, is the secondary data set of generally fainter stars for which it lists stellar positions at the epoch 2015, but no parallax or proper motions.

The DR1 positions were tested with numerous methods, including the comparison with external catalogues of sufficient precision (Arenou et al. 2017). The external validation of the astrometric accuracy of positions was made with two catalogues: the First U.S. Naval Observatory Astrometric Robotic Telescope (URAT1) catalogue (Zacharias et al. 2015) with a precision of positions 10–30 milli-arcsecond (mas), and with positions of quasars in the International Celestial Reference Frame (ICRF2) catalogue of quasi-stellar objects (Fey et al. 2015), and no deviations from the model of uncertainties adopted in DR1 were found.

Mignard et al. (2016) compared ICRF2 positions (Ma et al. 2009; Fey et al. 2015) of $G = 16-20$ sources with the auxiliary quasar table of DR1. They reported that if a comparison is made with the secondary data set of DR1, the dispersion of the normalised coordinate differences is about 30% higher than expected for the defining ICRF2 sources, probably because the positional uncertainties in DR1 are underestimated.

So far, no other validation of the DR1 secondary data set astrometry has been made at the mas-level because most external catalogues have insufficient accuracy. Here, we address this issue using CCD astrometric data sets obtained with the Focal Reducer and low dispersion Spectrograph 2 (FORS2) camera installed at the Very Large Telescope (VLT) as described by Lazorenko et al. (2014a). Our ground-based astrometry has a typical precision of 0.1–0.5 mas for individual stars. Comparison with DR1 is made by projecting its star positions into CCD space, computing the residuals of positions, and performing the statistical analysis of the scatter of these residuals. This investigation concerns only the random component of astrometric errors, because FORS2 astrometry is inherently differential and is applied to $G \simeq 16-20$ stars that are towards the faint end of the DR1 secondary data set. We also better characterise the distortion of the FORS2 camera, which allows us to re-calibrate the pixel scale and to update the parallaxes of ultracool dwarfs observed in our programmes.

2. Differential CCD data sets of FORS2 field stars

In 2010 we started an astrometric planet search targeting 20 ultracool dwarfs and very low-mass stars (Sahlmann et al. 2014, 2015a,b). Observations were obtained with the FORS2/VLT camera (Appenzeller et al. 1998), whose focal plane is

⋆ Based on observations made with ESO telescopes at the La Silla Paranal Observatory under programme IDs 086.C-0680, 087.C-0567, 088.C-0679, 089.C-0397, and 090.C-0786.

Table 1. Sky fields, root mean square (rms) of the positional differences between DR1 and FORS2 data sets, and average values of σ_G and σ_F for chip1.

	Comparison between DR1 and FOV					Comparison between DR1 and RF				
Nr	N	n	rms (mas)	$\langle\sigma_G\rangle$ (mas)	$\langle\sigma_F\rangle$ (mas)	N	n	rms (mas)	$\langle\sigma_G\rangle$ (mas)	$\langle\sigma_F\rangle$ (mas)
1	41	4	3.78	2.50	0.56	43	4	2.72	2.45	0.51
2	35	3	4.69	5.44	0.34	31	4	3.93	5.72	0.31
3	25	3	2.80	4.25	0.70	19	3	3.98	4.86	0.70
4	30	3	6.22	3.73	0.78	31	4	1.89	1.35	0.60
5	55	4	4.05	3.64	0.72	53	4	3.61	3.67	0.67
6	79	6	5.43	4.61	0.83	50	4	4.28	4.74	0.80
7	97	6	4.16	2.91	0.66	33	4	2.09	3.52	0.63
8	74	6	3.35	3.94	0.58	59	4	2.14	4.23	0.54
9	51	5	2.83	2.23	0.32	50	5	2.21	2.24	0.30
10	29	3	5.48	5.49	0.53	27	3	4.35	5.62	0.50
11	130	5	3.54	4.06	0.69	65	4	1.83	3.61	0.67
12	51	4	2.95	4.02	0.48	39	4	2.20	3.43	0.46
13	116	7	4.23	3.88	1.03	67	4	2.64	3.61	0.75
14	168	6	6.17	4.68	0.76	16	3	5.20	4.99	0.84
15	122	6	4.37	2.90	0.67	38	5	3.20	3.13	0.67
16	285	7	7.79	5.54	0.88	71	3	7.87	5.01	0.81
17	274	7	5.96	3.98	0.56	49	3	5.41	3.85	0.52
18	261	7	5.81	4.70	0.57	71	3	4.34	4.56	0.54
19	178	7	10.88	9.16	1.11	42	4	2.81	6.67	0.92
20	115	5	3.92	9.84	0.48	74	3	4.02	10.21	0.47

Notes. N is the number of common stars; n is the power of the fit model.

composed of two CCD chips. Images obtained with the high-resolution collimator have an approximate pixel scale of $s_0 = 0.1261''$/px (Lazorenko et al. 2014a). Our observations' design and reduction methods reach precisions of ~0.05–0.07 mas for $I = 15$–17 mag stars (Lazorenko et al. 2009, 2014a). Our CCD data setbased on observations in 2010–2013 contains images of $I \simeq 16$–22 mag stars in 20 fields close to the southern galactic plane, each covering $\sim 4' \times 4'$. The list of fields with a numbering adopted in Lazorenko et al. (2014a) is given in Table 1.

The main application of this data set is the search for reflex motion of the targets measured relative to the field stars in the plane of the sky. To ensure the best elimination of the atmospheric image motion and optical distortion of the telescope, the positions of the targets were computed relative to a reference frame formed by the dense grid of reference stars. The reference areas are circular and centred on the target. The reduction within each individual CCD image was made using a polynomial model with $M = (n + 1)(n + 2)/2$ basic functions per each CCD axis, which include full two-dimensional polynomials of x, y with the maximum power n, removing in this way the most important low-frequency components of the image motion spectrum (Lazorenko et al. 2009). Besides the reduction within the CCD plane, this model also takes into account the change of positions due to the proper motion, parallax, and colour effects.

2.1. RF data set of FORS2 field stars

A first supplementary result of the programme are the astrometric parameters of every star measured relative to the reference frame centred on the target ultracool dwarf: CCD positions x, y for the epoch 2011.38, proper motions in the CCD system, parallaxes, and chromatic parameters. The precision of our stellar positions $\sigma_F \sim 0.1$–1 mas is comparable to that of *Gaia* DR1 secondary data set, which is 0.1–20 mas (Gaia Collaboration 2016a), so we use the results of the $n = 4$ ($M = 15$) reduction for the current investigation. We will refer to it as the reference frame (RF) data set and it contains 6208 stars in 20 fields. There are two sub-sets, one per CCD chip.

The argumentation in the next sections relies on the fact that the system of these astrometric parameters is strictly homogeneous because it is defined by the same reference frame and basic functions. It means that for each RF star the differential x, y and the "absolute" x_{abs}, y_{abs} positions in some external catalogue given in the ICRF system, for example *Gaia*, are related by the expression

$$x_F - x_{abs} = F_n(x - x_{dwarf}, y - y_{dwarf}) + F_{noise} \quad (1)$$

along the X axis (the equivalent equation holds for the Y axis), where $x_F = -s_0(x - x_{dwarf})$ are the FORS2 positions expressed in units of arc and measured relative to the approximate position x_{dwarf} of the target, and $F_n(x - x_{dwarf}, y - y_{dwarf})$ is a sum of M two-dimensional basic functions of the maximum power n, with free model coefficients, which describe the transformation between the local reference frames in some sky fields and *Gaia* (Lazorenko et al. 2009). The term F_{noise} models random noise that is not correlated across the field. The variance of F_{noise} is equal to the quadratic sum of σ_F and the positional uncertainty in the external catalogue.

2.2. FOV data set of FORS2 field stars

A second result of these FORS2 observations is the astrometric parameters of stars obtained also with $n = 4$, but in a slightly different way. Specifically, each star was reduced with its own circular reference area. Therefore the locations of the reference frames are not fixed and move in the CCD plane. These individual areas cover the whole field of view (FOV) of the CCD and therefore we will refer to them as the FOV data set.

The system of astrometric parameters in the FOV data set is not exactly homogeneous because the set of reference stars is different for every star, thus we are using multiple reference frames. In comparison to RF, the FOV data set is larger and contains about 12 000 stars, because it includes stars outside the central reference areas aligned to the programme targets. These data were converted to the ICRF system using the US Naval Observatory (USNO-B) catalogue (Monet et al. 2003) and are available in the Strasbourg astronomical Data Center (Lazorenko et al. 2014b) as a deep catalogue of positions, proper motions, and parallaxes of faint stars in 20 sky fields. Because that conversion was based on USNO-B, the absolute precision of the astrometry degraded to ~0.2″, which is insufficient for a comparison with *Gaia* DR1. Therefore, to take advantage of the sub-mas precision of FORS2 differential astrometry, we instead used the original CCD positions and proper motions of FOV stars set by the reference frame fixed to the CCD pixels.

Both FORS2 data sets are based on exactly the same measured photocentres of star images and an identical reduction method, but differ in the reference frame definition. Although this difference may appear subtle, the discussion in Sect. 3 demonstrates that the RF positions are in better agreement with *Gaia*. We present the analysis of both data sets because the FOV data set has twice as many stars and therefore allows for a more robust comparison with DR1 positions.

3. Data analysis

We compared the positions of stars in *Gaia* DR1 that are in common with the RF and FOV data sets, which were converted from their average epoch 2011.5–2012.1 to the *Gaia* DR1 epoch

2015.0 using the proper motions measured with FORS2. These FORS2 positions refer to the barycentre of the solar system, because the proper motions and parallaxes were accounted for and atmospheric chromaticity parameters were incorporated into the astrometric model. The position uncertainties σ_F in 2015 were computed using the uncertainty and covariance matrix of the astrometric parameters of FORS2 stars, and include input from all known types of errors. The average value of σ_F over all sky fields is given in Table 1. Because the proper motions of FORS2 catalogues were obtained with a short timebase of about two years, the conversion between epochs significantly degraded the precision of FORS2 positions. For example, the typical precision for bright stars is roughly 0.1 mas for positions and 0.07–0.15 mas/yr for proper motions. After conversion to 2015, the proper motion errors propagated for a three and a half years difference increase the uncertainty of positions four-fold, to about 0.4 mas.

3.1. Error budget and unbiased rms of the residuals

We define the residuals, for example along the X axis, between FORS2 x_F and DR1 positions x_{abs} computed as a tangent projection to the CCD plane, as $\Delta = x_F - x_{abs}$ that indicates the left side of Eq. (1). The expected variance of the residuals is modelled by the sum $\sigma_G^2 + \sigma_F^2$, which includes the formal uncertainty σ_G of DR1 and the uncertainty σ_F of FORS2 positions at 2015. The average value of σ_F is 0.64 mas and small or comparable to σ_G for stars cross-identified with DR1. It is reasonable to assume that the measured variance of Δ can deviate from this model, and a more realistic error budget is

$$\sigma_\Delta^2 = \sigma_G^2 + \sigma_F^2 + \nu^2, \quad (2)$$

where we introduced an additional noise component ν to balance the discrepancy between the observed rms of the residuals and the nominal uncertainties in the catalogues. The ν component may be related to *Gaia* DR1 or FORS2 or both.

The problem is that the residuals Δ cannot be measured directly because x_F and x_{abs} are related by the polynomial relation in Eq. (1). While x_{abs} represents a flat coordinate system, the FORS2 positions x_F are affected by high-order geometric distortion. We therefore considered the corrected position residuals and the corrected residual rms. The corrections are based on the fact that the unbiased variance of the residuals $\hat{\Delta}_i = x_F - x_{abs} - F_n(x - x_{dwarf}, y - y_{dwarf})$ computed with the least squares fit of $i = 1 \ldots N$ measurements per axis for N common stars is $\sum \hat{\Delta}_i^2 w_i/(N - M)$, where M is the number of fit parameters and w_i are the weights which depend on a factor (e.g. on σ_G). For a limited sub-sample of $N' < N$ residuals in a narrow range of σ_G where the w_i are approximately constant, the unbiased estimate of the variance is $\langle\hat{\Delta}^2\rangle N/(N - M)$, where the angle brackets denote an average taken over N' measurements. Therefore the unbiased estimate of the residual rms is $\mathrm{rms} = \gamma\langle\hat{\Delta}^2\rangle^{1/2}$ where $\gamma = \sqrt{N/(N - M)}$ is a factor that compensates for the decrease in the degrees of freedom.

The original residuals Δ are affected by the least squares fit and cannot be restored exactly. However, they can be approximated by the corrected residuals $\Delta = \gamma\hat{\Delta} = \gamma(x_F - x_{abs} - F_n)$ with an unbiased variance. In the following discussion we deal with the bias-corrected rms and residuals Δ defined in this way.

3.2. Individual residuals between DR1 and FORS2

Equatorial star positions of DR1 stars were converted to Cartesian coordinates in the CCD plane using a tangent-plane projection. The reference point of the projection corresponded to the position of target objects, that is to the geometric centres of the RF data sets. Then we proceeded with stars whose uncertainty σ_G is better than 20 mas, cross-identified DR1 and FORS2 stars, and applied the polynomial model (Eq. (1)) to transform between these two sets of positions. The data for FORS2 chip1 and chip2 were reduced separately because the relative offset and orientation between the chips are known only approximately. Cross-matching between catalogues consisted in the initial rough identification of stars in a 1″ window and three iteration cycles of fitting the residuals Δ by polynomial functions of degree $n = 3$ and rejection of outliers over 60 mas. With two concluding iterations, detailed below, we obtained the final identification and derived the residuals Δ.

The main parameters of the fitting procedure are shown in Table 1. We present parameters for chip1 only because those for chip2 are similar, except for a smaller star number N and polynomial degree n. For every field and chip we had to choose the optimal polynomial degree n with number M of fit parameters. Naturally, an increase of M will lead to smaller residuals because there are more free parameters. Fitting polynomials with an arbitrarily high degree is undesirable and it is therefore necessary to identify the highest M for a particular data set. Since our model is linear and the errors are reasonably well-behaved, we used the F-test of additional model parameters, which yields the probability that the simpler model is true. This approach is described in detail by Sahlmann (2017) who applied it to the comparison between *Gaia* DR1 and *Hubble* Space Telescope (HST) observations of the *James Webb* Space Telescope (JWST) calibration field.

The weights in the system Eq. (1) of the transformation of FORS2 to DR1 were set to σ_Δ^{-2} initially computed with $\nu = 0$, which therefore assumes that the uncertainties σ_G and σ_F are good estimates. The stars were considered identified when the residuals in positions were within $5\sigma_\Delta$. Still, many stars were rejected as outliers because their residuals were slightly above the adopted five-sigma limit. The unusually high rate of outliers detected at this phase of identification, especially for stars with $\sigma_G < 1$ mas, indicates that the distribution of the residuals deviates from prediction (2). To obtain a more stable identification and to find a reasonable compromise between the number of identified stars and the rms of the residuals, we therefore computed the final weights in most fields with different values of $\nu = [0, 0.7, 1]$ mas.

3.3. rms of the residuals

The number of stars cross-identified with the RF and FOV data sets is 1421 and 3705, respectively, and the residual scatter is smaller for the comparison of DR1 with RF. To illustrate the statistics of the residuals, we computed for every field and FORS2 chip the rms of the residuals Δ and the (quadratic) average value of $\langle\sigma_G\rangle$ (see Table 1). These values are visualised in Fig. 1 and show an approximately linear correlation at $2 < \langle\sigma_G\rangle < 5$ mas where σ_G dominates over the other error components, including the FORS2 noise σ_F that has an amplitude below 1 mas (Table 1).

The rms is systematically higher for the residuals between DR1 and FOV in comparison to the residuals between the DR1 and RF data set, which is due to the difference of their

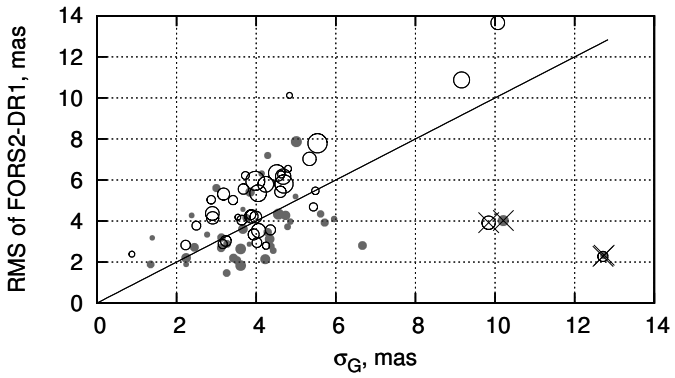

Fig. 1. Average rms of the residuals Δ between DR1 and FORS2 data sets FOV (open circles) and RF (grey circles) versus average value of σ_G for each sky field (field No. 20 marked by crosses) and each chip. The circle size is proportional to the number of stars, from 11 to 285.

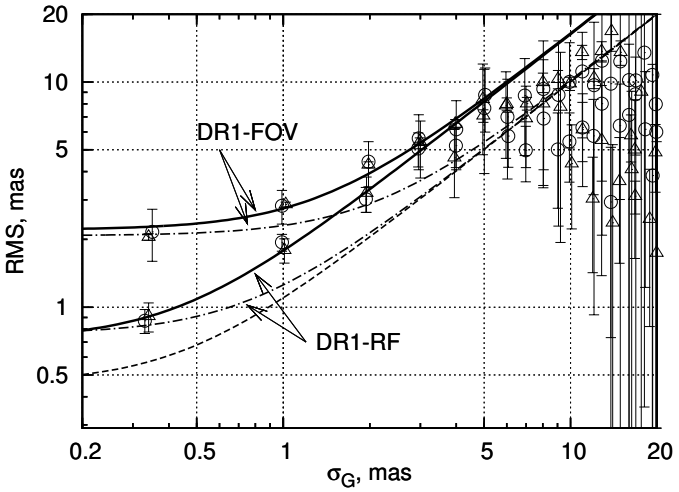

Fig. 2. rms of the positional residuals Δ between DR1 and FOV and between DR1 and RF for chip1 (circles) and chip2 (triangles) in every 1 mas bin of σ_G. Three-sigma error bars are drawn under the assumption of a normal error distribution. These data are compared with the model uncertainty σ_Δ computed with $\nu = 0$ in Eq. (2) (dashed lines) and with a value of ν that fits the rms at $\sigma_G < 0.5$ mas (dashed-dotted lines). Solid lines show the fit function Eq. (3).

construction as discussed in Sect. 2.2. We note that field No. 20 has unexpectedly small residuals at large σ_G.

We investigated how well the measured rms matches the model precision σ_Δ along a full range of $\sigma_G = 0 \ldots 20$ mas. For this purpose the residuals FORS2−DR1 were binned in 1 mas intervals of σ_G and quadratically averaged separately for every field and chip. The results presented in Fig. 2 demonstrate significant deviations from the model dependence Eq. (2) computed with $\nu = 0$ and shown by the dashed line, especially for $\sigma_G < 0.5$ mas. In that region, associated with brighter stars, σ_G and σ_F are much smaller than the measured rms values. This allowed us to derive a reliable estimate of ν by fitting the excess in rms with the expression (2). In this way we obtained $\nu = 2.04 \pm 0.11$ mas for the comparison of DR1 with FOV and $\nu = 0.66 \pm 0.08$ mas for the comparison of DR1 with RF. The significantly smaller excess ν in the latter case is a consequence of the more homogeneous astrometric system of the RF data set. The error component ν could be due to unaccounted excess noise in either DR1 or FORS2 astrometry, and the smaller value of 0.66 ± 0.08 mas can be put forward as an upper limit of ν potentially related to DR1. This estimate is strictly valid only for stars with G-band photometric magnitudes of 16.0–17.5, and average values of $\sigma_G \simeq 0.31$ mas and $\sigma_F \simeq 0.38$ mas. The value $\nu = 2.04$ mas obtained from the comparison of DR1 with FOV is likely caused by noise related to the multiple reference frames used in the compilation of the FOV data set (Sect. 2.2).

Since we determined the value of ν, Eq. (2) is fully defined in the range of σ_G and for any star sample we can compute σ_Δ, which models the expected value of the rms. The functional dependence of σ_Δ on σ_G is shown by the dashed-dotted lines in Fig. 2. The measured rms values now are well fitted with the model at $\sigma_G < 1$ mas. However, at $\sigma_G = 1-5$ mas we note a systematic positive bias of about a factor of 1.5, which remains constant in the logarithmic scale of the plot. Figure 2 suggests that the model (2) is not adequate in the $\sigma_G = 1-10$ mas range because here we found rms $> \sigma_\Delta$. In this interval, σ_G is much larger than the other noise components in Eq. (2), including ν and σ_F, which typically are 0.5–0.7 mas. Therefore, the discrepancy with the observations is likely due to an underestimated variance σ_G^2. We laid out the improved error budget

$$\sigma_\Delta^2 = A^2\sigma_G^2 + \sigma_F^2 + \nu^2 \quad (3)$$

with an additional parameter A that modulates the DR1 uncertainties. The two cases, $A > 1$ and $A < 1$ indicate that σ_G is under- and over-estimated, respectively. We fitted the complete sample of all residuals with this model, where we ingested both data sets of FORS2 and used three fit parameters: ν_{FOV} for the residuals "DR1"-"FOV", ν_{RF} for the residuals "DR1"-"RF", and A as a common parameter. The data were fit in the σ_G range 0−5.5 mas and produced the model parameters $\nu_{FOV} = 2.13 \pm 0.09$ mas, $\nu_{RF} = 0.44 \pm 0.13$ mas, close to the previous estimate, and $A = 1.63 \pm 0.05$. The fit approximates the observed data well for $\sigma_G < 5$ mas. At larger σ_G in the interval of 7–20 mas, the measured rms reaches a ceiling of about 5–8 mas, therefore Eq. (3) is not applicable there.

The solution of Eq. (3) differs between data sets in the range of $\sigma_G < 1$ mas because there σ_F is comparable to σ_G. We fit the observed rms in this region separately for both FORS2 data sets but obtained similar solutions for A. Therefore, we fit the combined (FOV and RF) data set with Eq. (3) and obtained $A = 1.83 \pm 0.07$, similar to the above result obtained in a wider range of σ_G. It means that Eq. (3) is applicable at least within a range of $0.5 < \sigma_G < 5$ mas and our results suggest that in this region the uncertainties of the DR1 secondary data set are underestimated.

We studied whether there is a difference in the residual rms for stars with large and small astrometric excess noise ε, which indicates the quality of the astrometric fit for every star in DR1 (Lindegren et al. 2016). The stars were divided into two groups with "large" and "small" ε as defined by a threshold value. Using different thresholds from 0.5 to 2 mas, we found no clear difference in the rms value for the subsets of stars, partly due to the small number of stars with large ε.

We found that Eq. (3) fits well the measured rms in every field, except for field No. 20 with an rms significantly below σ_Δ and three to five times smaller than σ_G. This field is unusual in terms of the stellar brightness and σ_G distributions. Whereas in most fields only ∼10% of stars have σ_G values of 10−20 mas, about half of the stars in field No. 20 have such large uncertainties. This is despite the fact that those stars are relatively bright ($G \simeq 17-19$) and should therefore have $\sigma_G \simeq 0.5-2$ mas as typical in the other fields. The reason for this peculiarity may be that *Gaia* observed this field less often, as reported by the average

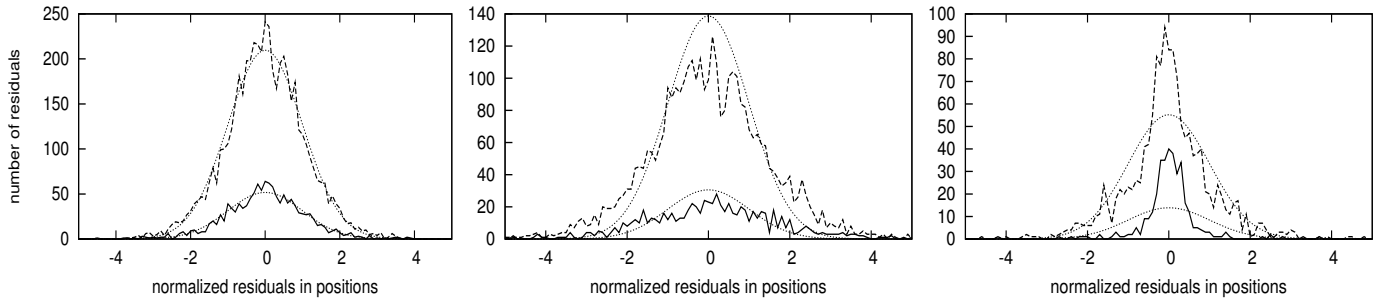

Fig. 3. Distribution of the normalised position residuals Δ between DR1 and RF (solid curves) and between DR1 and FOV (dashed curves) for stars with $1 < \sigma_G < 5$ mas. *Left panel*: the normalisation is based on σ_Δ computed with $A = 1.63$; *middle panel*: the same with $A = 1$; *right panel*: the same for stars with $\sigma_G > 7$ mas assuming that $A = 1$. The corresponding Gaussian distributions are shown by dotted lines.

number of good CCD observations in DR1 (catalogue entry *astrometric_n_good_obs_al*), which is smaller than for the other fields. Our findings therefore may demonstrate variations of the DR1 uncertainties in different areas in the sky.

3.4. Distribution of the residuals

The position residuals contain information on the distribution of DR1 errors, which can deviate from the normal law. Figure 3 shows the observed distribution of the residuals between FORS2 data sets and DR1 normalized to σ_Δ computed with the derived fit parameters. Because the uncertainty σ_Δ is correctly modelled by Eq. (3) only within a limited range of σ_G, we generated the histograms for stars in a conservative $1 < \sigma_G < 5$ mas range. We rejected residuals with large correction factors $\gamma > 1.3$, a situation usually related to sky fields with an insufficient number of identified stars N. The derived distributions follow a Gaussian distribution with no excess in the wings.

To demonstrate how the distribution shape depends on the value of A, we computed the uncertainties σ_Δ with $A = 1$ (that is, using the original uncertainties of DR1) and obtained the distributions in the middle panel of Fig. 3 with the best-fit estimates of ν_{FOV} and ν_{RF}. The difference relative to the left panel demonstrates the effect of the bias in the σ_Δ. Finally, we obtained the residual distribution for stars with $\sigma_G > 7$ mas (right panel). The strong concentration at zero indicates an overestimation of σ_G by at least a factor of two, as is also seen in Fig. 2.

3.5. Discussion

It is unlikely that the entirety of these results can be caused by errors in the FORS2 astrometry. For instance, excess noise ν can also originate if σ_G is correct but instead our value of σ_F is underestimated. For stars with $\sigma_G < 1$ mas the average value of σ_F is 0.41 mas. Increasing this value quadratically by $\nu = 0.44$ mas yields a new estimate of $\sigma_F = 0.73$ mas (78% over its nominal value), which removes the discrepancy between the measured and model variance of the residuals FORS2−DR1, while keeping σ_G untouched in this range. In this scenario, because σ_F is dominated by the uncertainty in proper motion, the 78% excess in our errors would refer almost entirely to FORS2 proper motions. However, applying the same argument in the range of $\sigma_G > 1$ mas, the excess noise ν cannot be due to underestimated FORS2 errors because that would lead to unrealistic manifold corrections to σ_F.

Potential sources of unaccounted noise in FORS2 positions are systematic errors in the measured photocentres of stars caused by imperfect modelling of the point spread function or from unmodelled blended light from nearby stars. We investigated other potential sources of the excess noise by looking for correlations between the residuals and brightness, position on the CCD, proper motion, and chromaticity parameters of individual stars. We did not find any significant correlation.

4. Update of the FORS2 pixel scale

The conversion of relative to absolute positions on the basis of *Gaia* DR1 allows us to derive the coefficients of the function $F_n(x - x_{dwarf}, y - y_{dwarf})$, which determine the optical distortions of the FORS2 camera, the perpendicularity of the CCD axes, the pixel scale and its variation across the CCD, and the differences of scales along X and Y directions. It is convenient to present Eq. (1) in the conventional form $s_0 x' - x_G = ax' + by' + x'_0 + \ldots$ and $s_0 y' - y_G = cx' + dy' + y'_0 + \ldots$, where $x' = -(x - x_{dwarf})$, $y' = y - y_{dwarf}$, and the high-order terms of the function F_n were omitted. Here we define the scale s and the coefficients of geometric distortion as

$$s = s_0 - (a + d)/2, \quad s_x - s_y = (d - a), \quad skew = (b + c), \qquad (4)$$

where $s_x - s_y$ characterises the scale difference between the two axes and the *skew* term gives information on the non-perpendicularity of those axes. Above expressions are applicable at the location of the target, where $x' = y' = 0$. In general, $s(x, y)$ and the other distortion coefficients are functions of field location and can be computed from the partial derivatives of F_n including the higher order terms (Sahlmann 2017).

The values of s for each sky field at the position of the target $x = x_{dwarf}$, $y = y_{dwarf}$ are given in Table 2 both for RF and FOV data sets. For comparison, the table contains scales s_0, which were previously derived on the basis of the USNO-B catalogue (Lazorenko et al. 2014a). Those scales were smaller than s_{FOV} and s_{RF}. This underestimation of the pixel scale was caused by the small degree of the polynomial transformation F_n that we used in Lazorenko et al. (2014a) that was fixed to $n = 3$ for all fields, but did not carry the x^2y and xy^2 terms because of the insufficient precision of USNO-B. Function F_n allowed for the transformation to ICRF with a precision of 40–70 mas, however, the absence of the x^2y, xy^2, and higher-order terms prevented it from resolving the field distortion. This is evident in Fig. 4, which shows how the scale $s(x, y)$ changes along the X axis of chip1 at $Y = 100$ px, close to the chip gap. The figure corresponds to the FOV data set, but it is nearly the same for the RF set. The function $s(x, y)$ is symmetric and reaches a maximum value of 126.33 mas at the chip centre (column $X = 1000$ px). The use of a simpler transformation F_n broadened the peak of

Table 2. Pixel scales, the skew and rotation parameters, and updated ultracool dwarf parallaxes ϖ.

Nr	DENIS-P	s_0 (mas/px)	s_{FOV} (mas/px)	s_{RF} (mas/px)	ϖ_0 (mas)	ϖ (mas)	*skew* (mas/px)	Rotation (mas/px)
1	J0615493-010041	126.17 ± 0.13	126.279 ± 0.006	126.295 ± 0.004	45.700	45.745 ± 0.112	0.034 ± 0.006	0.166 ± 0.013
2	J0630014-184014	126.20 ± 0.11	126.333 ± 0.013	126.329 ± 0.015	51.719	51.772 ± 0.099	0.002 ± 0.024	0.215 ± 0.017
3	J0644143-284141	126.10 ± 0.14	126.330 ± 0.005	126.331 ± 0.003	25.094	25.140 ± 0.094	–0.002 ± 0.004	0.193 ± 0.008
4	J0652197-253450	126.08 ± 0.12	126.265 ± 0.019	126.307 ± 0.006	62.023	62.135 ± 0.070	0.008 ± 0.010	0.206 ± 0.021
5	J0716478-063037	126.45 ± 0.14	126.355 ± 0.008	126.324 ± 0.005	40.918	40.877 ± 0.144	0.053 ± 0.009	0.201 ± 0.010
6	J0751164-253043	126.24 ± 0.12	126.325 ± 0.013	126.327 ± 0.004	56.304	56.343 ± 0.085	–0.030 ± 0.006	0.213 ± 0.015
7	J0805110-315811	126.07 ± 0.11	126.359 ± 0.013	126.337 ± 0.008	42.428	42.518 ± 0.083	0.015 ± 0.012	0.267 ± 0.015
8	J0812316-244442	126.01 ± 0.09	126.332 ± 0.008	126.322 ± 0.003	47.282	47.399 ± 0.094	0.048 ± 0.005	0.188 ± 0.014
9	J0823031-491201	126.26 ± 0.13	126.363 ± 0.018	126.331 ± 0.005	48.160	48.187 ± 0.190	–0.032 ± 0.006	0.203 ± 0.021
10	J0828343-130919	126.18 ± 0.09	126.353 ± 0.008	126.355 ± 0.006	85.838	85.957 ± 0.148	0.012 ± 0.017	0.170 ± 0.018
11	J1048278-525418	126.01 ± 0.08	126.339 ± 0.008	126.345 ± 0.003	36.212	36.308 ± 0.077	0.101 ± 0.005	0.268 ± 0.013
12	J1157480-484442	126.23 ± 0.11	126.344 ± 0.014	126.354 ± 0.005	34.633	34.667 ± 0.082	0.009 ± 0.012	0.223 ± 0.021
13	J1159274-524718	126.32 ± 0.06	126.352 ± 0.010	126.322 ± 0.003	105.538	105.540 ± 0.120	–0.012 ± 0.007	0.202 ± 0.014
14	J1253108-570924	126.00 ± 0.10	126.274 ± 0.026	126.207 ± 0.034	60.064	60.163 ± 0.054	–0.093 ± 0.038	0.128 ± 0.026
15	J1520022-442242	126.08 ± 0.09	126.321 ± 0.017	126.316 ± 0.009	53.995	54.096 ± 0.109	0.057 ± 0.018	0.239 ± 0.023
16	J1705474-544151	126.12 ± 0.07	126.358 ± 0.011	126.293 ± 0.011	37.549	37.601 ± 0.087	0.041 ± 0.017	0.205 ± 0.018
17	J1733423-165449	126.46 ± 0.09	126.355 ± 0.013	126.333 ± 0.010	55.272	55.216 ± 0.073	0.037 ± 0.016	0.174 ± 0.016
18	J1745346-164053	126.09 ± 0.26	126.299 ± 0.010	126.294 ± 0.006	50.871	50.953 ± 0.096	0.034 ± 0.010	0.201 ± 0.018
19	J1756296-451822	125.97 ± 0.12	126.244 ± 0.025	126.318 ± 0.011	43.577	43.697 ± 0.064	0.194 ± 0.018	0.247 ± 0.040
20	J1756561-480509	126.30 ± 0.13	126.292 ± 0.018	126.266 ± 0.008	47.039	47.026 ± 0.058	–0.018 ± 0.012	0.184 ± 0.019
	Median	126.14 ± 0.11	126.336 ± 0.010	126.323 ± 0.008			∼0	0.202 ± 0.016
	Luhman 16	126.10 ± 0.11	126.329 ± 0.010		500.51	501.419 ± 0.11		

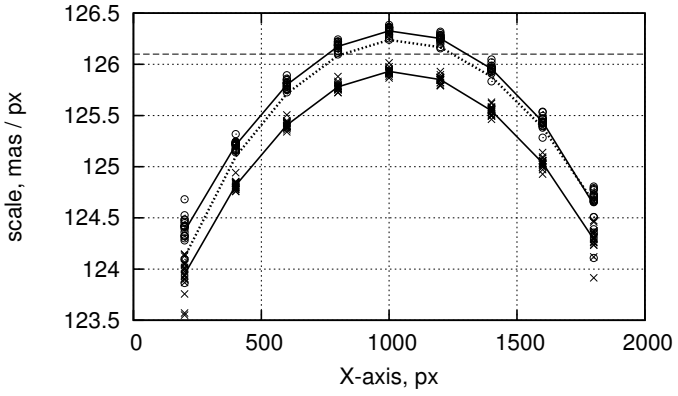

Fig. 4. Change of FORS2 pixel scale s in chip1 along the X axis for each sky field at Y = 100 px (open circles) and at Y = 500 px (crosses). The average scales (solid curves), the scale obtained by Lazorenko et al. (2014a, horizontal dashed line), and the scale s computed with use of distortion coefficients in chip 2 at Y = 0 (dotted curve) are shown.

$s(x, y)$ and yielded the lower value of 126.1 mas reported in Lazorenko et al. (2014a).

The function F_n represents the difference between the local reference frame and *Gaia*, but not directly between the star positions in the CCD system and *Gaia*. This induces additional distortions in the differences $x-x_{\rm dwarf}$ and $y-y_{\rm dwarf}$ and is the reason why the individual values of s are scattered by over three sigma (see Table 2). In particular, the scatter of points in Fig. 4 is due to this effect. Figure 4 shows that the scale changes across the chip and in the outer regions of Y = 500 px are about 0.5 mas/px lower compared to at Y = 100 px. This confirms that the conversion from pixel to angular units should be done with a scale evaluated at the position $x = x_{\rm dwarf}$, $y = y_{\rm dwarf}$ of the target. In our observations $x_{\rm dwarf}$ and $y_{\rm dwarf}$ varied by ∼100 pixels for different targets, thus adding additional scatter in the measured scale (Table 2) because that is a function $s(x, y)$.

The pixel scales in chip 1 and chip 2 of FORS2 cannot be directly compared because they are modulated by the optical distortion. To investigate possible scale differences between chips, we used the coefficients of F_n of chip 2 and computed $s(x, y)$ at the dividing gap between the chips, where F_n is still applicable. These scales correspond to Y = 0 in chip 1 (dotted curve in Fig. 4) and are in good agreement with scales at the nearby location defined by Y = 100 px. Attributing the common curved shape to the optical distortion and the offset to the separation in Y, we find no scale discontinuity between the two chips.

The *skew* parameter given in Table 2 shows that the axes' non-perpendicularity is small (0.01–0.02 mas/px) and consistent with zero. However, it formally varies by over three sigma between the sky fields due to the skew of the local reference frames. The difference $s_x - s_y$ shows a similar random scatter with an average close to zero. This disagrees with our former estimate of -0.37 ± 0.06 mas/px (Lazorenko et al. 2014a), possibly for a reason similar to the discussed difference of the pixel scale.

The Flexible Image Transport System (FITS) headers of FORS2 indicate a relative rotation of 0.083° between the two CCD chips. We verified this by evaluating the coefficients of the function F_n. For chip 1, we find the inclination $\theta_1 = (b - c)/2$ between the ICRF and the axes of the FOV reference frames at the position of the target, which approximately corresponds to the inclination between the ICRF and the CCD axes. We used the function F_n for chip 2 to determine the inclination θ_2 about 200 px below the target. Instead of b and c we used their exact local values computed with the partial derivatives of F_n. The difference $\theta_1 - \theta_2$ between the inclination angles is the rotation between the chips, which is given in Table 2 for each field. Its

median value is (0.202 ± 0.016) mas/px, thus the Y axis of chip 1 is rotated clock-wise relative to that of chip 2. This corresponds to a rotation of (0.092 ± 0.009)° and agrees with the value given in the FITS headers.

5. Updated parallaxes of ultracool dwarfs

With the now better-determined pixel scales, we corrected the (absolute) parallaxes ϖ_0 of 20 ultracool dwarfs reported in Sahlmann et al. (2014) that were computed with scales s_0 given in Table 2 by applying a multiplicative factor $\beta = s/s_0$. We used scales obtained in individual sky fields to take into account variations related to the local reference frames. We used $s = s_{\rm RF}$ because of the better internal precision, but the factors β computed with $s = s_{\rm FOV}$ are nearly the same. The applied β factors vary from 0.9990 to 1.0028, thus the corrections are small and change the parallaxes ϖ by about 0.1 mas, comparable to the formal parallax uncertainties.

The effect is more significant for the binary brown dwarf WISE J104915.57−531906.1 (LUH16, Luhman 2013). By analysing the FORS2 images obtained by Boffin et al. (2014) we derived the relative (500.23″) and absolute parallax ϖ = 500.51 ± 0.11 mas of this system located ∼2 pc from the Sun (Sahlmann & Lazorenko 2015). Using HST observations in 2014–2016, a pixel scale determined on the basis of *Gaia* DR1, and the parallax correction of Sahlmann & Lazorenko (2015), Bedin et al. (2017) derived the relative and absolute parallax of LUH16 of 501.118 mas and 501.398 ± 0.093 mas, respectively, significantly larger than the values of Sahlmann & Lazorenko (2015). Applying the correction factor β computed with s_0 = 126.1 mas from Sahlmann & Lazorenko (2015) and s = 126.329 ± 0.010 mas, which is the median of the complete set of $s_{\rm FOV}$ and $s_{\rm RF}$, we obtained the updated relative 501.139 mas and absolute ϖ = 501.419 ± 0.11 mas FORS2 parallax of LUH16, in agreement with Bedin et al. (2017).

6. Conclusion

We compared the predicted and measured residual rms in position between the *Gaia* DR1 and FORS2 astrometric data sets of 20 astrometric fields. The relationships between these two data sets are non-trivial and require the introduction of an auxiliary term ν to take into account the excess in the residual scatter. In addition, the behaviour depends on the *Gaia* position uncertainty $\sigma_{\rm G}$ and is different in the ranges smaller than 5 mas and larger than 7 mas. Our study is sensitive to the random component of position errors that are uncorrelated on spatial scales of about 2−4′ because of the limitations of the FORS2 differential astrometry. Our results apply to the faint end of the *Gaia* DR1 content, that is to stars with $G > 16$.

In the range of $\sigma_{\rm G}$ = 0.5−5 mas, our results suggest that the actual value of the DR1 uncertainty is underestimated by 63% for 80% of stars typically fainter than G = 17. This conclusion agrees with the finding of Mignard et al. (2016, Appendix A), on the uncertainty of the *Gaia* DR1 secondary data set. In contrast, we find that for $\sigma_{\rm G} > 7$ mas, that is mostly $G > 20$ stars, the actual DR1 uncertainties are overestimated by a factor of two.

The excess noise ν in our model was detected primarily in the residual rms of G = 16−18 stars with $\sigma_{\rm G} < 0.5$ mas. This noise could originate from *Gaia* DR1 and/or from FORS2. We cannot pinpoint the likely source, but we determined that the component related to *Gaia* DR1 cannot exceed 0.44 ± 0.13 mas, which corresponds to $\nu_{\rm RF}$ for the RF data set. We expect that the situation will be clarified with the second *Gaia* data release that will provide us with astrometry of even higher quality.

Finally, the availability of the *Gaia* astrometry allowed us to more precisely calibrate the geometric distortions of our extensive FORS2 data sets, to derive a better pixel scale, and consequently update the parallaxes of the 20 ultracool dwarfs in our planet search programme and that of the LUH16 binary. Whereas for most of our targets the correction is smaller than 0.1 mas, the updated FORS2 parallax of the LUH16 system is larger by about 1 mas. This demonstrates the value of the accurate, optically faint, and dense reference frame that *Gaia* provides for high-precision ground-based differential astrometry.

Acknowledgements. This work has made use of data from the ESA space mission *Gaia* (`http://www.cosmos.esa.int/gaia`), processed by the *Gaia* Data Processing and Analysis Consortium (DPAC, `http://www.cosmos.esa.int/web/gaia/dpac/consortium`). Funding for the DPAC has been provided by national institutions, in particular the institutions participating in the *Gaia* Multilateral Agreement.

References

Appenzeller, I., Fricke, K., Fürtig, W., et al. 1998, The Messenger, 94, 1
Arenou, F., Luri, X., Babusiaux, C., et al. 2017, A&A, 599, A50
Bedin, L. R., Pourbaix, D., Apai, D., et al. 2017, MNRAS, 470, 1140
Boffin, H. M. J., Pourbaix, D., Mužić, K., et al. 2014, A&A, 561, L4
Casertano, S., Riess, A. G., Bucciarelli, B., & Lattanzi, M. G. 2017, A&A, 599, A67
Fey, A. L., Gordon, D., Jacobs, C. S., et al. 2015, AJ, 150, 58
Gaia Collaboration (Brown, A. G. A., et al.) 2016a, A&A, 595, A2
Gaia Collaboration (Prusti, T., et al.) 2016b, A&A, 595, A1
Gaia Collaboration (Clementini, G., et al.) 2017, A&A, 605, A79
Lazorenko, P. F., Mayor, M., Dominik, M., et al. 2009, A&A, 505, 903
Lazorenko, P. F., Sahlmann, J., Ségransan, D., et al. 2014a, A&A, 565, A21
Lazorenko, P. F., Sahlmann, J., Ségransan, D., et al. 2014b, VizieR Online Data Catalog: J/A+A/565/A21
Lindegren, L., Lammers, U., Bastian, U., et al. 2016, A&A, 595, A4
Luhman, K. L. 2013, ApJ, 767, L1
Ma, C., Arias, E. F., Bianco, G., et al. 2009, IERS Technical Note, 35
Mignard, F., Klioner, S., Lindegren, L., et al. 2016, A&A, 595, A5
Monet, D. G., Levine, S. E., Canzian, B., et al. 2003, AJ, 125, 984
Sahlmann, J. 2017, Astrometric accuracy of the JWST calibration field catalog examined with the first Gaia data release, Analysis Report JWST-STScI-005492, STScI
Sahlmann, J., & Lazorenko, P. F. 2015, MNRAS, 453, L103
Sahlmann, J., Lazorenko, P. F., Ségransan, D., et al. 2014, A&A, 565, A20
Sahlmann, J., Burgasser, A. J., Martín, E. L., et al. 2015a, A&A, 579, A61
Sahlmann, J., Lazorenko, P. F., Ségransan, D., et al. 2015b, A&A, 577, A15
van der Marel, R. P., & Sahlmann, J. 2016, ApJ, 832, L23
Watkins, L. L., & van der Marel, R. P. 2017, ApJ, 839, 89
Zacharias, N., Finch, C., Subasavage, J., et al. 2015, AJ, 150, 101